PREDICTING DRUG DELIVERY EFFICIENCY INTO TUMOR TISSUES THROUGH MOLECULAR SIMULATION OF TRANSPORT IN COMPLEX VASCULAR NETWORKS

by
Evan Troendle

A thesis submitted to Johns Hopkins University in conformity with the requirements for the degree of Master of Science in Engineering

Baltimore, Maryland

April, 2017

Abstract

Efficient delivery of anticancer drugs into tumor tissues at maximally effective and minimally toxic concentrations is vital for therapeutic success. At present, no method exists that can predict the spatial and temporal distribution of drugs into a target tissue after administration of a specific dose. This prevents accurate estimation of optimal dosage regimens for cancer therapy. Here I present a new method that predicts quantitatively the time-dependent spatial distribution of drugs in tumor tissues at sub-micrometer resolution. This is achieved by modeling the diffusive flow of individual drug molecules through the three-dimensional network of blood-vessels that vascularize the tumor, and into surrounding tissues, using molecular mechanics techniques. By evaluating delivery into tumors supplied by a series of blood-vessel networks with varying degrees of complexity, I show that the optimal dose depends critically on the precise vascular structure. Finally, I apply my method to calculate the optimal dosage of the cancer drug Doxil into a section of a mouse ovarian tumor, and demonstrate the enhanced delivery of liposomally administered doxorubicin when compared to free doxorubicin. Comparison with experimental data and a multiple-compartment model show that the model accurately recapitulates known pharmacokinetics and drug-load predictions. In addition, it provides, for the first time, a detailed picture of the spatial dependence of drug uptake into tissues surrounding tumor vasculatures. This approach is fundamentally different to current continuum models, and reveals that the target tumor vascular topology is as important for therapeutic success as the transport properties of the drug itself. This sets the stage for revisiting drug dosage calculations.

Acknowledgements

I express my deepest gratitude to my thesis advisor, Dr. Martin Ulmschneider, for his drive, guidance, and support throughout the years. His perseverance and integrity has propelled me to think critically and has enabled me to achieve my scientific goals not limited to this thesis. I would like to thank my fantastic lab members, Charles Chen, Hayden Fennell, Dr. Yukun Wang, and Zafirah Liyana Abdullah for our day-to-day interactions and cultivation of new ideas.

I thank the entire faculty members and staff at department of Materials Science and Engineering and the Institute for NanoBioTechnology at Johns Hopkins for their support. I have been inspired by their words of encouragement and through their interactions within our departments. I definitely need to thank my undergraduate advisors from the Coe College physics department. Without the encouragement and discipline of Dr. Mario Affatigato, Dr. Ugur Akgun, and Dr. Steve Feller, I would likely have only made it an order of magnitude less as far.

I would like to thank my parents, Erin Soteco and Joseph Troendle, and my sister, Caitlyn Troendle for their support throughout the years. I am eternally inspired by their strength, their energy, and their support for me in all matters.

Last but certainly not least, I would like to thank my family, Samantha Obman and my two ‘children’, Luna the lovely feline, and Francesco the betta. Without the loves of my life, it would truly be utterly dismal, and I am thankful for every day I spend together. Please accept the fruits of my education towards the fulfilment of our wondrous lives together.

This project has been supported by a pilot grant from the Johns Hopkins Institute for NanoBioTechnology to my advisor, Martin B. Ulmschneider, (CCNE Pilot Project Grant #90058409).

Table of Contents

List of Tabless

List of Figures

Introduction

Knowledge of the efficiency of drug delivery from the vasculature into target tissues is important for estimating the optimal dosage regimen for a given drug[1]. This is particularly significant for anticancer drugs, which typically have narrow therapeutic windows[2,3].

Drug dosing for humans is often derived from animal studies, which are refined in human clinical trials[4]. Adaptation to individual patients is achieved by scaling the standard dose based on weight or body surface area (BSA) using empirical calculations, with the DuBois and Mosteller formulas being the most commonly used[5]. BSA based regimens have been criticized, as they cannot account for the 4 to 10-fold variation in drug clearance typically observed within any particular patient pool[6]. In cancer patients calculations based on these methodologies have resulted in both increased toxicity due to overdosing[7] as well as decreased efficacy and possible development of drug-resistance due to underdosing during chemotherapy[8]. This highlights the need for better tools to predict doses that fall within the therapeutic window[9].

Systemic delivery of therapeutics into tissues relies upon the vascular network, which also delivers oxygen and nutrients. In healthy human tissues (e.g. liver, kidney, muscle), cells are typically located ~50 µm from a blood vessel[10], which results in good tissue distribution of pharmaceuticals with high permeability. In contrast, drug delivery into tumor tissue is complicated by the leaky and defective tumor vasculature. The growth of the neovasculature recruited to supply tumor cells is typically slower than the proliferation rate of cells inside a tumor[11,12]. This results in a significant increase in the average normal distance to the nearest vessel for cancer cells (>100 µm) and a lower overall density of blood vessels inside a tumor[13,14]. Together with reduced lymphatic drainage, this creates an acidic and hypoxic extracellular environment for tumor cells at larger distances from the vasculature due to accumulation of byproducts of cell metabolism (e.g. lactic acid and carbonic acid) and oxygen starvation[15]. Targeting cells in these deeply buried microenvironments with chemotherapy is challenging, because drugs may not diffuse efficiently enough through the interstitial space to reach them[16], and the drugs that do reach deep into these tissues may be less active due to the acidic microenvironment[17].

The ability of anticancer therapeutics to come into contact with all proliferating cells within a non-operable tumor is vital for prolonging remission or preventing relapse. To improve delivery into solid tumors nanoparticle-based cancer drugs have been developed that exploit the enhanced permeability and retention (EPR) effect[18] by penetrating the leaky junctions of the tumor vasculature and accumulating inside tumor tissues[19].

Simple drug delivery models typically divide the organism into a number of compartments such as blood vessel, peripheral tissue, and tumor tissue. How much of a given compound was delivered to the tumor is calculated by assigning first order rate constants to model the transport between the various compartments and by taking into account clearance[20,21]. While these models can be parameterized to capture uptake in the tumor microenvironment implicitly, the spatial resolution of the drug in the target tissue and hence the overall effectiveness of a particular chemotherapeutic dose remain undetermined.

Models that incorporate the spatial distribution of a drug have applied continuum finite-element[22] and finite-difference methods[16], fluid-mechanics formalisms[23,24], and time evolution of differential equations[21,25,26]. These models generally treat both the blood vessels and the tissue as a homogeneous continuum. While this approach works well for simple systems, solving the boundary conditions of realistic vascular structures, which are typically highly complex, is computationally prohibitive. Thus, no model currently exits that can capture the complexity of the physiological micro-environment of tumors, such as the structure of the blood vessels, and the preferential uptake of drugs and nutrients by particular regions within the tumor.

Here, I present a new method that predicts the spatial drug delivery efficiency into a target tissue. To achieve this, I simulate the diffusive transport of compounds through a vasculature towards target tissues using molecular mechanics methods in complex geometrical volumes. The model works for both molecular solutes as well as nanoparticle-based delivery systems that carry thousands of individual pharmaceutically active compounds.

Methods

Modeling the vasculature, endothelium, and surrounding tissues

Stochastic drug transport towards target tissues is modeled by pseudo-random diffusion through a micrometer-resolution three-dimensional (3D) model of vasculature and surrounding tissue (see Figure 1). Corrosion casts and micro-computed tomography (μCT) scans of tumor vasculatures show branched networks of arteries, capillaries, and veins that are approximately cylindrical in cross section[13]. In order to capture the vascular network efficiently I modeled veins and arteries as linked cylinders of constant radius, with a sphere at either end to allow modeling of bends and branches as well as changes in radius (see Figure 1). This greatly facilitates tracking of drug diffusion through the various compartments representing the vasculature and surrounding tissues, which makes the simulation of a large number of particles tractable with reasonable computational effort.

Tissues surrounding the vasculature are modeled as rectangular prisms that are connected in three-dimensions. This allows calculation of the spatial distribution of drug flow and concentration in tissues. For the present study, I have assigned the particle diffusivity to be isotropic for the vasculature and tissues. However, different diffusivities in x, y, and z can be assigned for each element of the tissue or vasculature (e.g. dependent of vessel radius or related to the distance from the closest vessel), and there is no major computational overhead associated to adding microscopic structural features, such as individual tumor cells or blood lakes, to these tissues. While the tissue mesh allows for full spatial and temporal tracking of particle concentrations within tissues, the particles themselves are able to move freely in three dimensions and their position is not constrained by the grid (Figure 1A).

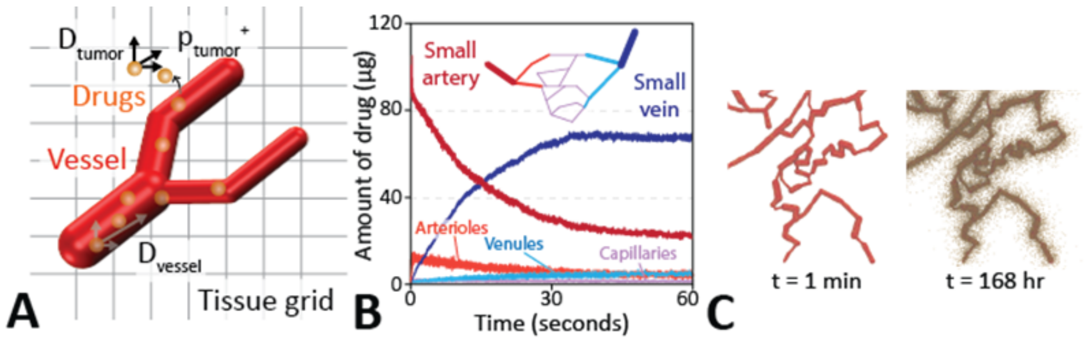

Figure 1 | Drug diffusion model schematic and drug equilibration inside the vasculature. A. A three-dimensional tissue model is created by mapping of the vasculature and surrounding tissues onto simple geometric shapes (cylinders, spheres, and a cubic grid) that allow rapid computational boundary determination. The vasculature is modeled as a chain of cylinders, connected via spheres that allow branching as well as changing of the direction and radius of blood vessels. Interstitial space and target tissues are represented as a cubic grid. Drugs are represented by individual particles that diffuse through the system under the influence of Brownian motion, with the diffusion constant depending on the location of the drug (i.e. vessel or tissue). Drugs incident on the walls of the vasculature are transferred back and forth between the vessel and the tissue with a given probability via a kinetic Monte Carlo scheme. The probability, p_+^{tumor}, of drug transport from blood vessels into tumor tissues was determined from rate constants provided in a multicompartment model. **B.** Kinetics of drug equilibration within the vascular network shown in the inset. The blood vessel components are small arteries (red), arterioles (light red), capillaries (pink), venules (light blue), and veins (blue). The figure demonstrates rapid equilibration of an injected drug dosage throughout the vasculature. **C.** Two frames show an evolution of a simulation trajectory. Drugs (brown) transfer out of the vessel and disperse into the tissue. As only a small number of particles leave the vessel at each simulation step, particle concentrations remains high in vessels.

Drug delivery system

Here I study both the delivery and transportation of the molecular anticancer drug doxorubicin and Doxil, an FDA-approved liposomal formulation of doxorubicin. Doxil liposomes are around 100 nm in diameter and PEGylated to reduce uptake by the MPS and increase clearance half-time[20]. The initial distributive pharmacokinetic phase of doxorubicin has a half-life of ~5 minutes, whereas the terminal elimination half-life ranges between 20-48 minutes[27]. Conversely, Doxil's distributive phase is approximately 5 hours and has an elimination half-life of between 47 and 59 hours.[28] The pharmacokinetic profile of Doxil suggests that the liposomes are largely confined to the vasculature during the distributive and eliminative steady-states, whereas free doxorubicin is rapidly absorbed by tissues and leads to a large volume of distribution with considerably more side-effects due to indiscriminate tissue uptake[20,29]. Both doxorubicin and Doxil are well-studied chemotherapeutics allowing comparison to previous pharmacokinetic models and clinical data. Temporal release of drugs from liposomes has been measured *in vitro*[30,31] and described via mathematical models,[32] roughly following an exponential decay of drug released over time.

Drug diffusion in the vasculature and surrounding tissues

Diffusion of the drugs and the delivery system was modeled by a fixed step-size spherical random walk in combination with a Metropolis Monte Carlo scheme to hop between vasculature and surrounding tissues (summarized in Figure 1). A time-step of $\Delta t = 1$ second was chosen with a fixed Einstein diffusion length (i.e. step-size) inside the vasculature of $\sqrt{(6D\Delta t)}$ in a spherically random direction.

For the vasculature a diffusion coefficient of $D_{vasc} = 1.0x10^{-7}$ cm^2/s was chosen for Doxil, which corresponds to the theoretical random diffusion of a spherical liposome of 100 nm diameter through capillary blood. For the small molecule drug doxorubicin $D_{vasc} = 1.0x10^{-5}$ cm^2/s was chosen, which is the same order of magnitude as other molecules of similar size. Regarding the surrounding tissues, diffusivity measurements *in vivo* are challenging at present. The diffusion length of doxorubicin inside the interstitial space of tumor tissues was chosen to be $D_{tiss} = 1.0x10^{-9}$ cm^2/s. This value is consistent with a drug that delivers well in tissues with dense vasculature. The diffusive lengths of nanoparticles are certainly much lower. The diffusivity of Doxil liposomes was based on measurement of a nanoparticle of similar size and mass in a collagen matrix. Many nanoparticles diffuse on the order of 10^{-13} cm^2/s in tissues , but the selection of $D_{tiss} = 1.0x10^{-12}$ cm^2/s is closer line with previous simulations of Doxil, and yields a similar drug penetration in the tumor, due to the square root dependence on diffusivity on permeation length.

For the present study, I model only diffusive flow of liposomes through the vasculature, across the endothelium, and into and across surrounding tissue. Time-dependent blood flow and viscosity, as well as more fine-grained tissue structures can be implemented straightforwardly to refine this model. I show below that equilibration inside the vasculature is much faster than trans-endothelial transport and diffusion in surrounding tissues. Thus, flow was ignored for the present study. Further confidence in the characterization of diffusive measurements is vital to the success of the model.

Transendothelial transport

Tumor endothelium has leaky junctions between cells, resulting in increased transport of large complexes including liposomes up to around 500 nm in diameter[33–35]. This can be modeled by adjusting the permeability for individual segments of the vasculature. Since I are simulating the delivery of individual molecules rather than using a continuum representation, the first-order rate constant for transport between compartments must be converted into a per-particle transport probability.

This is achieved using a kinetic Monte Carlo approach. In brief, the experimentally determined first-order rate constant of a drug exiting a compartment (e.g. Doxil moving from blood into tumor tissue) was converted to a corresponding Monte Carlo probability for this process. The probability of trans-endothelial transport was determined from fitting to pharmacokinetic data for Doxil (Figure 3A). This probability, p_{trans}, is obtained by equating the number of molecules or nanoparticles $N(t)$ in a vessel at some time $t = n\cdot\Delta t$ ($n = 0,1,2,\ldots$) calculated by transforming a first-order pharmacokinetic rate equation:

$$N(n\Delta t) = N_0 e^{-k\cdot n\Delta t} \qquad \text{(Eq. 1)}$$

into a Monte Carlo population decay equation:

$$N(n\Delta t) = N_0 (1 - p_{trans})^{n\Delta t} \qquad \text{(Eq. 2)}$$

Here N_0 is the initial population, k is the first-order rate constant, n is the number of simulation steps, and Δt is the time-step passed in the simulation, and p_{trans} is the Monte Carlo probability of a change of state (i.e. transport event or clearance event). The solution of this equation gives the rate-derived transport probability:

$$p_{trans} = 1 - e^{-k\Delta t} \qquad \text{(Eq. 3)}$$

Converting the rate constant into a Monte Carlo probability in this approach is compatible with existing pharmacokinetic compartment models (Figure 3A).

It is important to note that pharmacokinetic compartment models, which follow Eq. 1, contain no information on particle proximity to the vessel walls and hence assume that all particles can potentially exit the compartment at each simulation step. While this works well for clearance, it is a poor approximation for transport across the endothelium (Figure 3B).

In a structural model, such as the one presented here, the final location of a molecule in the system depends on the precise trajectory through the vasculature and surrounding tissues. Only molecules within a volume element surrounding the vascular surface may traverse the endothelium. For each cylindrical vascular segment this volume element is: $\Delta V = c \cdot v_{av} \cdot \Delta t$, where v_{av} is the mean speed of the drug in the blood vessel, and c is a constant that depends on the geometry of the vessel segment. This limits the fraction of drugs which can possibly leave each vessel within the next simulation step (Figure 3C). The sum of all volume elements of the vasculature scales non-trivially with the total volume of the entire compartment (i.e. the blood vessel). This leads to improper scaling of the rate-derived probability (Eq. 1), which would ultimately need to be scaled in each vascular segment to perfectly match a compartmental model. For fixed transport probabilities (e.g. p_{tumor}, $p_{\text{clearance}}$, p_{tissue}, p_{delivery}), the final delivered dose scales linearly with the surface area to volume ratio (Figure 3F), i.e. delivery depends on the three-dimensional structure of the vasculature. Figure 3 demonstrates that incorporating surface area contributions, as in my present particle-based model, is essential for calculating delivery levels.

At present, my model makes no assumptions about the mechanisms of trans-endothelial transport. However, mechanistic and physiological details such as increased permeation within predefined leaky endothelial regions or vessel sub-sections can be implemented without loss of efficiency. Furthermore, anisotropic diffusivities in different vessel segments, drag forces, and other biases can be straightforwardly incorporated.

Drug injection, clearance, and delivery

Injection is simulated by placing all drug molecules at a point source in the artery and equilibrating to uniform concentration throughout the vasculature, before enabling trans-endothelial transport and clearance. Clearance by macrophages, liver, and kidneys is simulated as a random removal using a kinetic Monte Carlo scheme with rate $k_{clearance}$.

Delivery from the large vessels (arteries or veins) into surrounding tissues is modeled using a kinetic Monte Carlo approach outlined above (Eq. 2) with a rate constant of $k_{delivery} = (k_{clearance} / 100)$. This value is based on the observation of a much slower clearance (plasma half-life $t_{½} > 180$ hrs) of fluorescently loaded nanoparticles and free drug within mouse tissues when compared to the normalized plasma bound concentration of nanoparticles and free drugs[36–39]. Delivery and accumulation are visualized by recording the total number of liposomes in target areas and tissue cross sections, as well as plotting their time evolution, peak and average concentrations, and area under the curve (Figure 2).

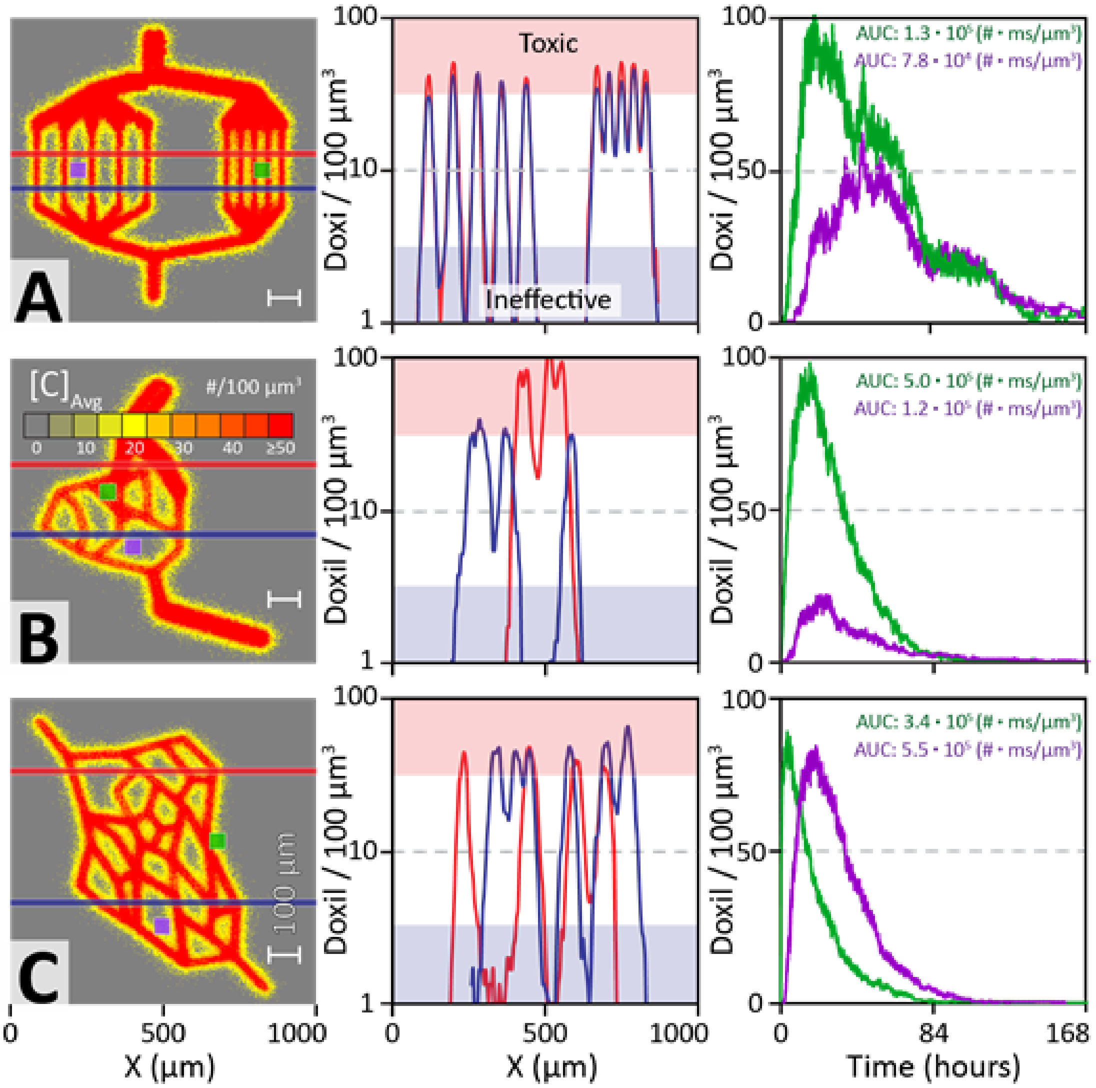

Figure 2 | Simulated drug delivery into model tissues of different complexity. Each panel in the first column shows a heat map of the final drug concentrations at the end of a simulation with shared parameters. Each vasculature is embedded in a tissue grid of 300x300x300 voxels with a linear dimension of 1 mm, resulting in a voxel volume of 37.0 µm^3. The second column shows the final drug concentration through two different linear cross sections of the tissue (red & blue indicated in the first column), while the third column shows the time-dependent drug concentration at two target sites within the tissue (green & purple indicated in the first column). After injection of 10^6 drug particles into a source artery, each system was equilibrated by allowing particles to diffuse freely throughout the vasculature without allowing their exit into surrounding tissue. The therapeutic window of the drug is indicated for the cross-sectional profiles (red = toxic, blue = ineffective). **A.** Drug delivery into a simple vasculature model composed of parallel capillaries with 50 µm, and 100 µm spacing, representing healthy and tumor tissue averages, respectively. The concentration cross-section shows that narrow capillary spacing (i.e. healthy tissues) result in good drug delivery with all sections falling into the therapeutic window, while increasing the capillary distance results in therapeutic gaps between the capillaries. The pharmacokinetics at target sites in the middle of two capillaries shows an up to 50% smaller area under the curve for tumor tissues as well as a lag in reaching peak concentration. **B.** Drug delivery into a simple branched micro-tumor model with uneven capillary spacing. While the average capillary spacing is very similar to the parallel tumor tissue in panel A, the two-dimensional nature of the capillary network results in much larger regions that are outside the therapeutic window in the cross-sectional analysis. A target site with a close proximity to a variety of vessels shows very high drug loads, whereas a site embedded near the center of large loops receives a five times lower dose. **C.** A more complex branched and looped planar capillary web model, shows similar behavior than the branched model in panel B. This figure highlights that vessel geometry greatly influences drug delivery efficiency. Choosing a target site that is located further away from the capillaries in an acute angle (purple) shows better drug delivery, despite a time-lag for drugs arriving at the site, compared to a site situated closer to the capillaries by in an obtuse branching angle (green).

Results

Equilibration in the vasculature

A human red blood cell takes less than one minute to circulate through the body[40]. For a small molecule or delivery vehicle suspended in blood, this means that equilibration inside the vasculature is orders of magnitude faster than diffusion across vessel walls. Since my model does not currently include blood flow, solute molecules and nanoparticles are first equilibrated inside the vasculature. This prevents biasing the simulation results with respect to the injection site. Figure 1B shows that random diffusion alone is sufficient to equilibrate the concentration in the vasculature within 10,000 ms. I found that all vasculatures tested here efficiently equilibrated within 10 minutes CPU time for an injection of 1 million liposomes. This corresponds to $5\mathrm{x}10^{-9}$ of a typical dose of 100 mg of Doxil within a simulation volume of a 1 mm^3 microtumor, corresponding to $\sim 1\mathrm{x}10^{-8}$ the volume of an average human body.

How vascular structure impacts tissue penetration

Figure 2 shows diffusion of doxorubicin through three vascular structures of different complexity. To simplify visualization, analysis, and model validation, all vasculatures in the present study are constructed in a plane. However, all vasculatures exist as full three-dimensional objects and my model and software implementation does not require them to be confined to a plane.

Tissue cross-sections (second column of Figure 2) show that, as expected, the maximum drug concentration declines steeply with distance from the nearest capillary. The overall distribution of drugs throughout the tumor tissues depends directly on the localized spacing of capillaries. As expected, delivery into tissue regions that are far removed from blood vessels is poor, while delivery into well-vascularized tissues is high. For example, for parallel capillaries increasing the spacing from 50 µm[13,14,41], which corresponds to the mean spacing of healthy tissues to 100 µm[13,14,42,43], which is a low mean spacing for tumors, reduces the total delivered dose by a factor of 6 (Figure 2A).

The third column in Figure 2 shows the time-evolution of the drug concentration within two target regions over the course of the delivery simulation. Numerical integration provides the pharmacokinetic area under the curve for each target area. These plots show that the time-evolution of the concentration, peak concentration, area under the curve, and rates of change vary with the distance of the target area relative to the vasculature.

Cross-sections of more complex branched vasculatures reveal a similar general trend (Figure 2BC), but show that the average spacing of capillaries is a poor predictor of drug delivery. Instead, the distance-weighted vascular volume surrounding a target tissue is the key indicator of delivery efficiency. Indeed, drug concentrations are particularly high at the branching points of capillaries. In the proximity of small branching angles (<30°) concentrations are approximately triple compared to similar distances of straight capillaries, and are still 15% larger at 90° branches. This is due to a higher vessel surface to tissue volume ratio close to an angled vessel.

Pharmacokinetics

Grouping the key structural features of the spatial tumor model into individual compartments (i.e. vasculature, tumor tissue, peripheral tissues, and clearance) allows direct comparison of my model with both experimental pharmacokinetic measurements as well as previous kinetic models. Figure 3A shows clinical measurements of the blood concentration of Doxil at various times after injection[29]. The data show that Doxil is not cleared rapidly, reflecting the long clearance half-time. Figure 3A shows that these data can be used to calibrate clearance parameters for a simple four-compartment model (blood, tumor, peripheral tissue, and clearance), developed by Wong et al.[20] as well as the equivalent clearance kinetics predicted by my new structural model.

Drug clearance data is typically available from clinical studies that measure the mean blood concentration of drugs in patients as a function of injection dosage[8,29]. However, plasma concentrations can differ by over one order of magnitude within hours of monitoring between individual patients[6]. In the present study, I fitted the drug concentration in blood to clinical clearance data from patients that were injected with 25 or 50 mg/m^2 of Doxil[29], respectively to obtain the clearance rate, in agreement with previous studies[20].

Unfortunately, the clinical clearance rate does not allow estimating the rate of uptake for tumor and peripheral tissue. To estimate the total amount of drug accumulated in the tumor Wong et al. explored a range of different rate constants for peripheral tissue and tumor uptake (k_+^{tissue}, k_+^{tumor}) and efflux (k_-^{tumor}, k_-^{tissue})[20]. Figure 3B shows that in the absence of a three-dimensional vasculature (i.e. using the stochastic Monte Carlo approach to move drugs between structure-less compartments) the time dependent accumulation of drugs in tumor predicted from the four-compartment model can be replicated quantitatively. The variation of the EPR effect (i.e. varying the ratio of k_+^{tumor} to k_-^{tumor}) can also be replicated if diffusion of all drugs into the tumor is considered in the absence of structural information (Figure 3C).

However, for a three-dimensional vasculature and tumor tissue model the functional form of Doxil accumulation, as well as the amount in the tumor tissue is different from the compartment model (Figure 3D). This is due to an oversimplification of the compartment model, which moves any particle with the same probability to a new compartment, irrespective of its location in the vasculature or tissue. This ignores the fact that the probability to cross into the surrounding tissues is dependent on location and flow dynamics. This effect is particularly prominent for vessels with larger diameters, as the transport probability for a structural model scales approximately with the surface area of the vessel (i.e. the number of particles near the vessel walls), while compartment models scale with vessel volume (i.e. the total number of particles).

The uptake kinetics and total amounts delivered differ significantly between structural and structure-less models (c.f. Figure 3BD). Remarkably, comparison of the time-dependent uptake kinetics of Doxil in all three vasculatures shown in Figure 2 was found to be similar in functional form (Figure 3E), yet the ultimate dose delivered is different for all vasculatures. This shows that pharmacokinetics alone are poor indicators of effective drug doses at target sites and cannot provide information on how evenly drugs are distributed within a tumor. The total amount of drug delivered into the tumor scales approximately with the surface to volume ratio of the vascular network embedded into the tissue (Figure 3F), highlighting the importance of vascular structure for drug delivery.

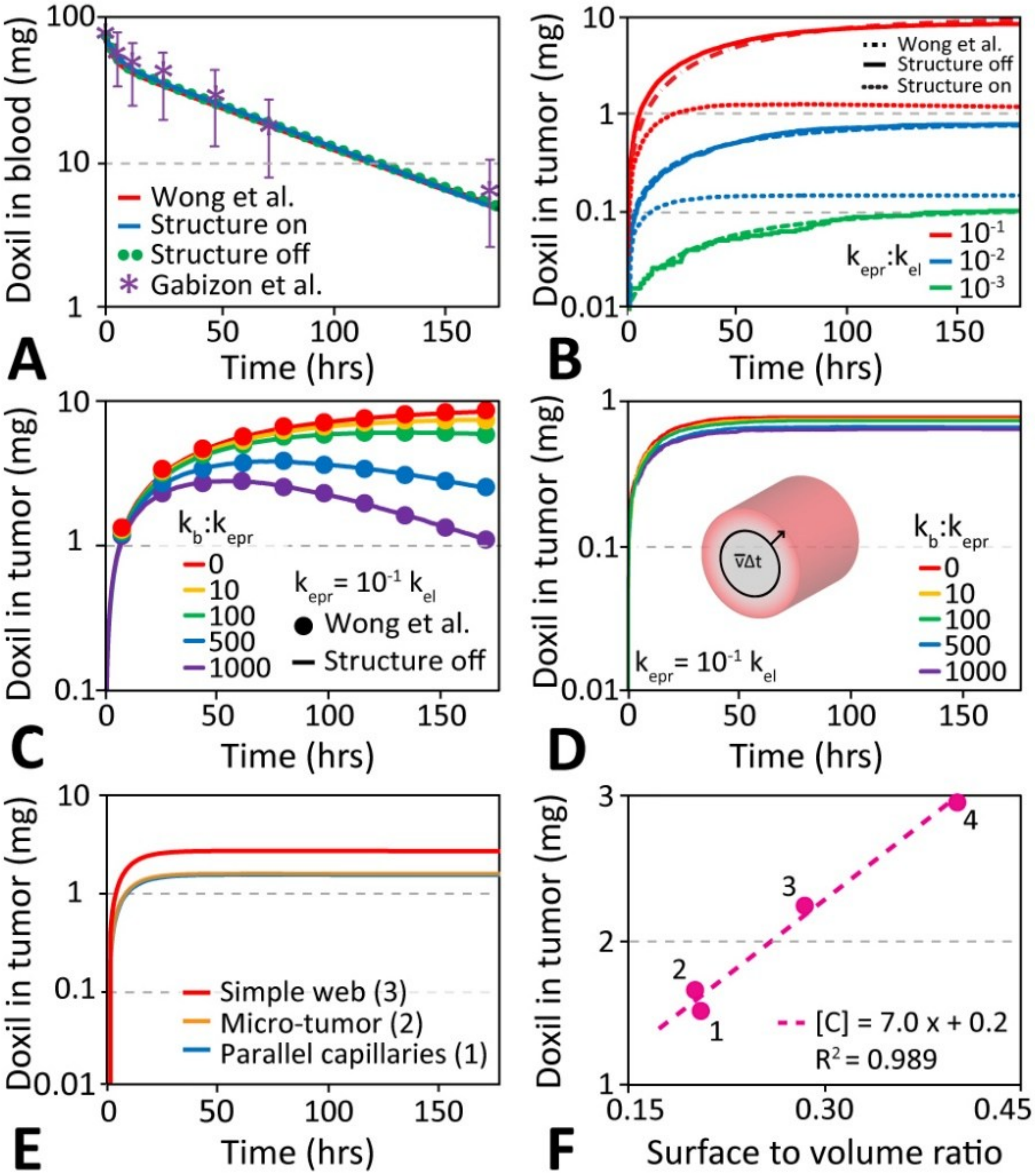

Figure 3 | Compartment-based pharmacokinetics of Doxil delivery into tumors. A. Comparison of the time dependence amount of Doxil in blood (i.e. the total vasculature) after injections of 50 mg/m^2 from clinical data (Gabizon et al.), a multi-compartment model (Wong et al.), a spatial compartment model: 'structure off' (i.e. drugs were moved in and out of the 3D vasculature without regards to their physical position), and the spatial model presented in this study: ‘structure on’. All three models are able to reproduce the clinical data. **B.** Time dependent uptake of Doxil in the tumor for different ratios of k_+^{tumor}:$k^{elimination}$, which quantify the strength of the EPR effect. The functional form of the drug uptake modeled by the compartment model proposed by Wong at al., (dashed line) can be reproduced for a 3D blood vessel compartment if all drugs leave the vessel with identical probability (“structure off”, shown as a solid line). However, when only drugs incident on the vessel wall may cross into surrounding tissues, the shape of the curve changes and the number of drugs reaching the tumor decreases by an order of magnitude. **C.** In the compartment model, and when the position of the drug in the vasculature is not taken into account, the concentration of Doxil over time depends on the ratio of the transport into (k_+^{tumor}) and out of (k_-^{tumor}) the tumor for a given ratio of k_+^{tumor}:$k^{elimination}$. **D:** When the position of the drug inside the vasculature is taken into account the dependence of drug delivery into tissues on the back-transport rate (k_-^{tumor}) is almost negligible. The overall functional shape is different from the compartment model (panel C), and the total drug uptake is an order of magnitude smaller. This difference arises from the volumetric modeling of the vessel, which restricts transport across the endothelium to drugs that are within the volume element $\Delta V = c \cdot v_{av} \cdot \Delta t$, where v_{av} is the mean speed of the drug in the blood vessel, and c is a constant that depends on the geometry of the vessel segment. This result implies that the structure cannot be ignored and that extravasation is more likely than intravasation, since the solid angle of a capillary is small compared to the surrounding tissues for a drug near a vessel. **E:** Comparison of the time-dependent uptake of Doxil in the three vasculatures shown in Figure 2, with identical simulation parameters. The absolute dose delivered into the tumor varies between the three systems. **F:** The surface to volume ratio of the all vasculatures scales linearly with the delivered peak concentration for the vascular structures in Figure 2. The least-squares linear regression trend-line suggests that [C], the amount of therapeutic delivered to the tumor, is roughly scales with x, the surface-to-volume ratio of the vascular network embedded into the tissue. This shows the importance of vascular structure in delivery when providing uniform kinematic variables (i.e. tissue diffusivity and trans-endothelial probabilities) in the context of different vascular systems.

Transendothelial transport and tissue diffusivity

As outlined in Figure 3, drug delivery into a tumor depends strongly on clearance kinetics from blood, diffusivity within the tumor tissues, and transendothelial permeability. Accurate spatial mapping of drug delivery into tumor tissues requires realistic parameters for these quantities. Figure 4 shows the effect of variation in transendothelial permeability and tissue diffusivity for a fixed clearance rate. The figure demonstrates graphically that while transendothelial permeability is vital in getting drugs into the tumor, tissue diffusivity is the key determinant for efficient delivery into deeply buried tissues.

Comparison of the delivery of Doxil, modeled as spherical particles with 100 nm diameter with a tissue diffusivity of 10^{-12} cm^2/s, transendothelial permeation probability of $6.33\text{x}10^{-5}$ s^{-1}, and clearance rate of $k = 2.28\text{x}10^{-3}$ hr^{-1}, with doxorubicin (1.7 nm diameter, tissue diffusivity = 10^{-9} cm^2/s, transendothelial permeation permeability =

4.36×10^{-4} s^{-1}, clearance rate of $k = 1.57$ hr^{-1}) reveals that doxorubicin, due to its small size penetrates much deeper into the tumor tissues than Doxil (see below).

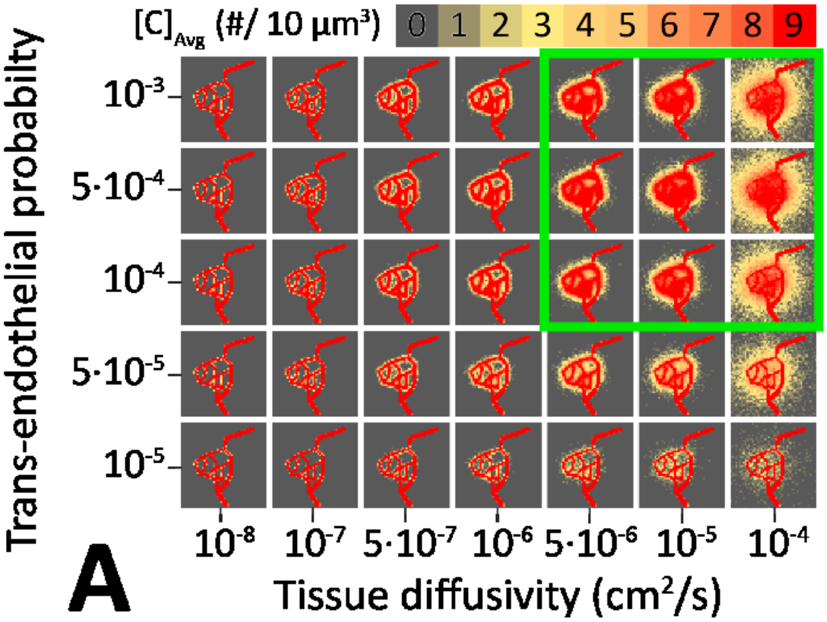

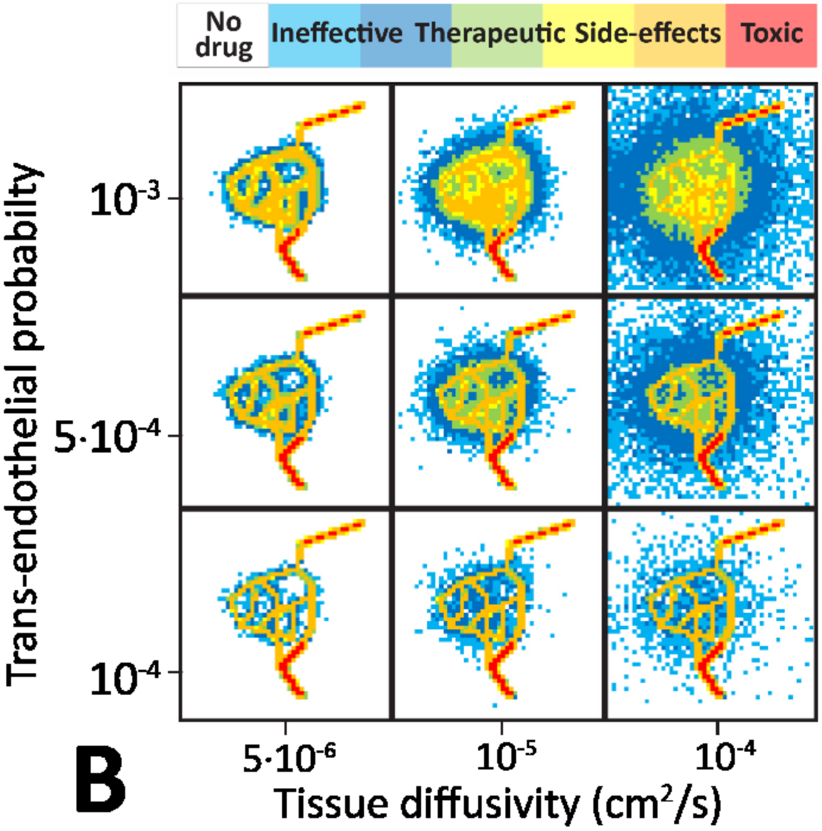

Figure 4 | Three-dimensional final distribution of drugs in tumor tissues as a function of the trans-endothelial transport probability and tissue diffusivity of drugs in the tumor. A: A heatmap plot shows the number density of drugs inside the vasculature and diffused into the tissue at the end of the simulation for different ranges of trans-endothelial transport probability and tissue diffusivity. Systematic exploration of these two properties allows narrowing down the pharmacological transport features required for a drug to be delivered efficiently into a tissue supplied by a given vasculature. For the vasculature shown in this figure the optimal range of parameters is highlighted by a green box. Outside this parameter range the structure of the vasculature effectively prevents delivery of drugs at sufficient concentrations to treat the tumor.
B: Analysis of the drug distribution across the tumor tissue allows precise spatial mapping of the therapeutic efficiency. For each row the total number of drugs released into the tissue is approximately constant. However, the diffusive length into the tissue varies with an expected square-root-dependence of the diffusion coefficient. Thus, tissue diffusivity, rather than trans-endothelial transport propensity is essential for increasing the volume of tissue within the therapeutic window.

Delivery of doxorubicin through a realistic tumor vasculature

Tumor vasculatures have complex structures, which are abundant in chaotically branched microvessels that form loops and dead ends[13,14,44–46]. These malformed vascular networks typically have microvessels that vary greatly in diameter when compared to healthy tissues. Often there is no preferred blood flow direction or the vasculature is connected only to feeder arteries with no draining veins[47]. To explore the effect of these structural features on drug delivery I modeled the vasculature of a mouse ovarian tumor by tracing the tumor capillaries from a positron emission tomography (PET) scan (Figure 5A)[48].

Figure 5 shows that equilibration in the complex vasculature is rapid and the complexity of the vascular network branching itself presents no barrier to delivery as the drug distributes uniformly throughout the vessels within 180 seconds. Simulation of spontaneous drug diffusion out of this vasculature shows that the key barrier to delivery is the spacing of the blood vessels. This means that not all regions of the tumor reach drug concentrations that fall within the therapeutic window. While regions close to the vasculature are generally well saturated by doxorubicin, many regions buried deeply inside the tumor tissue remain effectively untreated with few or no drugs reaching this far. Increasing the injection dose to treat these deeply buried parts of the tumor tissue may result in toxic side-effects, thus rendering portions of the tumor untreatable for drugs with insufficient tissue diffusivities.

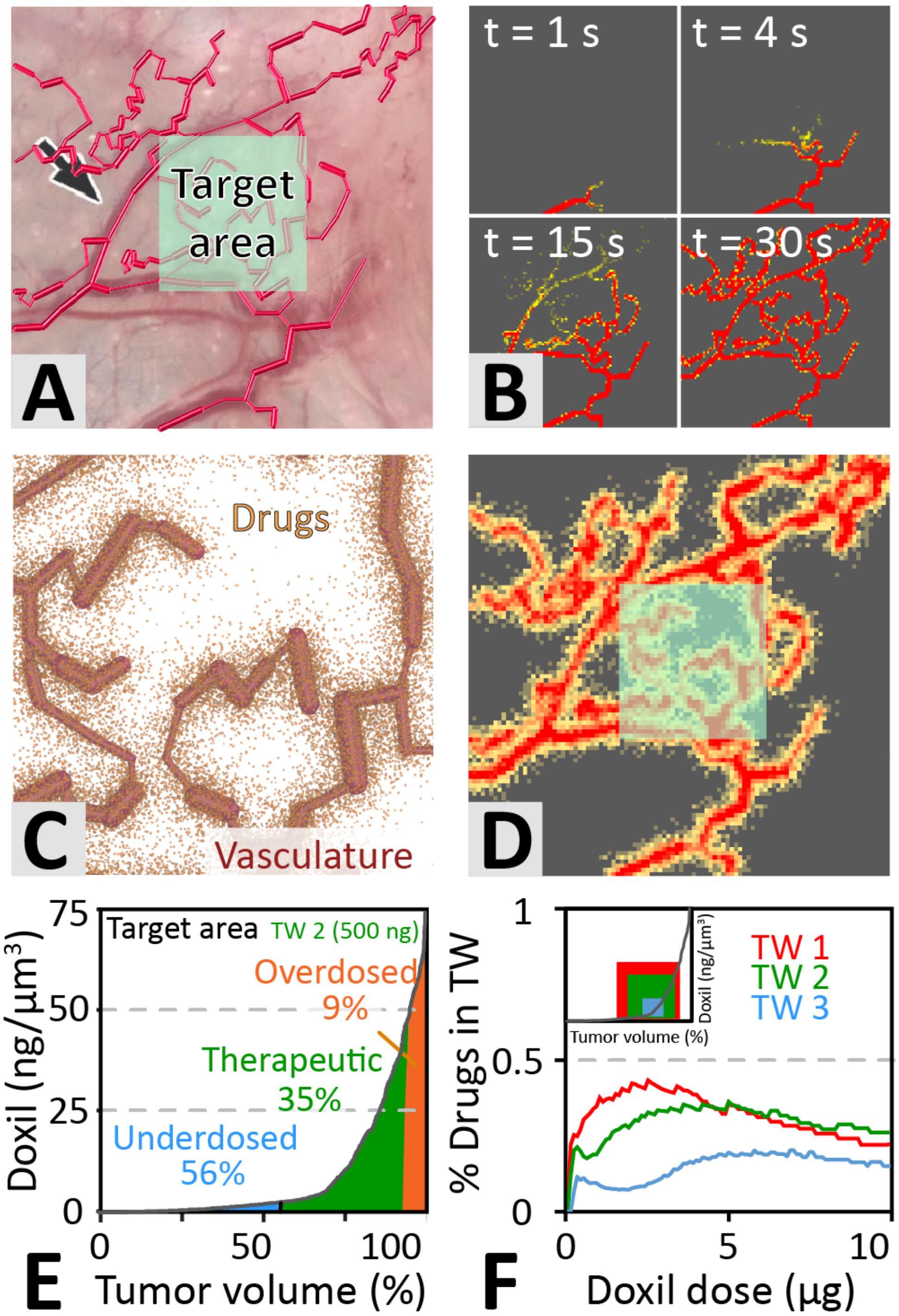

Figure 5 | Application of the three-dimensional molecular mechanics model to a realistic vascular system. A. The tumor vasculature was modeled by tracing blood vessels from an image of a mouse ovarian tumor seven days after subcutaneous injection. Only a subset of the tumor was modeled for simplicity and the trace was turned into a three-dimensional vascular structure. **B.** After injection into the main feeder artery drugs were allowed to diffuse across the vasculature. Equilibration, even for a complex vasculature like this one is typically completed within 30 to 60 seconds. **C.** After equilibration in the vascular network drugs start to slowly diffuse across the endothelium into the surrounding tissues. The figure shows the position of drug particles at the end of a 168-hour simulation with an initial dose of 10 million liposomes (equivalent to 5 ng of doxil). **D.** A heat-map of drug concentration in the tissue (300x300x300 voxel mesh) surrounding the vasculature reveals the spatial distribution of drugs in the various regions of the tumor. **E.** Analysis of larger sub-volumes within the tumor tissue (the target area highlighted in panels A and C), allows precise mapping of the therapeutic efficiency predicted. For the shown injection dose of 10 million drug particles (i.e. Doxil liposomes) ~35% of the target tissue reached a dose of doxorubicin within TW 2 (see **F**) and ~45% of the total target area was sufficiently saturated with drugs to kill tumor cells. **F.** The inset includes three therapeutic windows, TW 1, TW 2, and TW 3, which denote a wide, intermediate, and narrow therapeutic window, respectively. The initial dose was sequentially iterated between 0 and 10 nanograms of Doxil, to determine the percentages of the drugs within the therapeutic window. The effects of the therapeutic window, drug kinematic properties, and vascular structure are all important to consider when determining the success of a proposed dosage.

Dosage optimization

Drugs like doxorubicin have a permeability of at least 10^{-9} cm^2/s and a transendothelial transport probability of approximately 10^{-6} when there a collision with blood vessel walls given a simulation time step of 1 second. Improving therapeutic efficacy (i.e. increasing the tumor volume within the therapeutic window) can be achieved by enhancing the transendothelial transport rate and tissue diffusivity. In general, the optimal dose depends on a maximal tumor volume obtaining drug concentrations within the therapeutic window, which is constrained by the tumor vasculature. Figures 5 & 6 show optimized doses for a specific target area within a tumor. These have been calculated using the scheme for dosage optimization in Figure 6. Optimal dosimetry depends on all inputs to my model (i.e. vascular and tissue fine-structure, trans-endothelial transfer probabilities, tissue diffusivities, clearance rates, and therapeutic window). The initial dose was increased iteratively to discover the optimal dose in both target areas. The optimal dose for the targets shown in Figures 5 & 6 with a therapeutic window of 5-50 pharmacophores per 37 μm^3 is around 2.5 and 10 ng/mm^3 of tumor, respectively. These dosages result in 35-43% of the target volume receiving a dose within the therapeutic window.

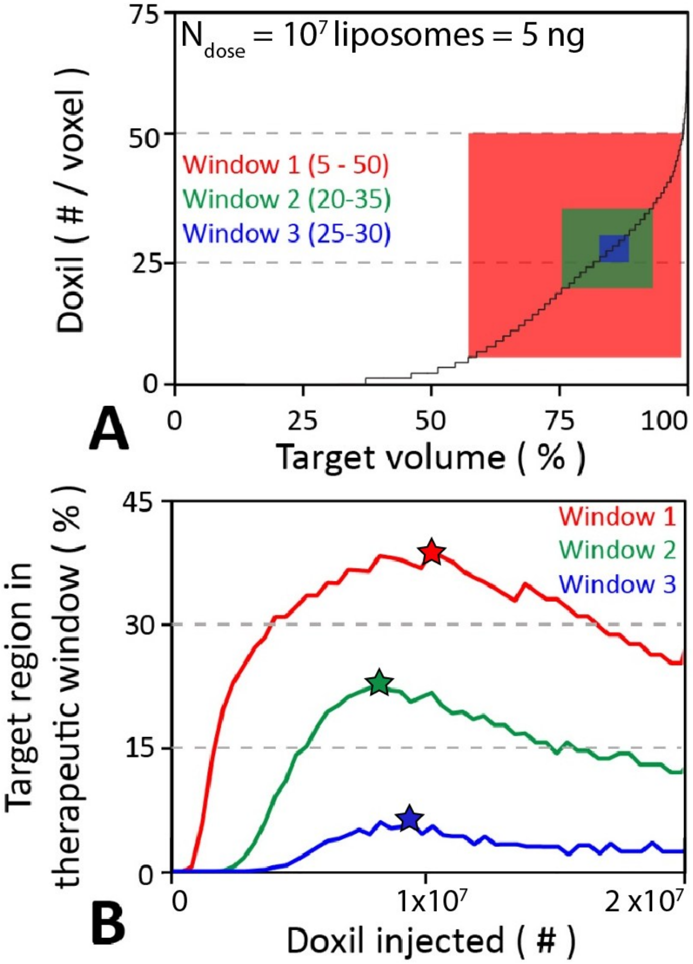

Figure 6 | Optimizing the volume within different therapeutic windows for a target area in a tumor tissue. A. The concentrations within the voxels inside a different target area from Figure 5 sorted in ascending order. The initial injection was of 10,000,000 particles for the entire system. The resulting curve shows the percentage of voxels with a given concentration at the end of the simulation. Three therapeutic windows were proposed: large (window 1: 5-50 doxorubicin per 37 µm^3 voxel), medium (window 2: 20-35 doxorubicin per voxel), and narrow (window 3: 25-30 doxorubicin per voxel). Rectangles representing the window are overlaid, where the height of the rectangle represents the width of the therapeutic window, and the width of the rectangle represents the percentage volume of the tumor with concentrations within that window. **B.** Percentages of therapeutic dose in the target tissue are plotted with respect to the number of Doxil liposomes injected at the beginning of the simulation. The procedure to discover the optimal dose was iterated involved many simulations with initial injections of 0 to $2x10^7$ Doxil in $5x10^4$ increments, by calculating the horizontal width of the therapeutic window at the end of the simulation (t = 168 hrs). Maximum therapeutic intensities vary and are denoted by stars, which is demonstrative of the arduous fine-tuning which can be possible for drugs of various toxicities and kinematics to be optimally effective within a given vascularization of a tumor.

Comparison of doxorubicin payloads via liposomal and direct doxorubicin administration

I calculated the tumor delivery efficiency of equivalent molar quantities of doxorubicin via injection of two different formulations: Doxil liposomes and doxorubicin molecules (Figure 7). Injection of $9.6x10^5$ Doxil liposomes (approximately 0.5 ng with parameters above), resulted in approximately 1% of the dose accumulating in the tumor over the course of 168 hours (Figure 7AD). The tissue penetration depth (i.e. average distance of a Doxil molecule from the surface of the nearest blood vessel) per Doxil was 10.7±8.7 micrometers. The final locations of each Doxil that reached the tissue was then replaced with 50 doxorubicin molecules, each simulated as a single doxorubicin molecule, but statistically representing 1000 doxorubicin molecules being released from the Doxil liposome. The resulting dispersion of doxorubicin resulted in minimal back-transfer into the blood stream (less than 3%), and a resulting dose of ~50 pg doxorubicin to the tissue, with average tissue penetration of 46.5±29.4, micrometers (Figure 7BD). The amount of doxorubicin cleared in blood from both Doxil and Doxil-released doxorubicin clearance was 0.495 ng.

In contrast, direct injection of $5x10^6$ doxorubicin molecules (again each representing 1000 molecules) in uniform concentration throughout the vasculature resulted in a dose delivered to the tumor of ~18 pg, and the an average tissue penetration of 46.0±29.1 micrometers, with 0.498 ng of the dose being cleared by blood (Figure 7CD).

This demonstrates that injection of Doxil more than doubles the dose of doxorubicin delivered into the tumor, while tissue penetration and clearance of doxorubicin remain roughly identical. However, clearance of doxorubicin is on the timescale of minutes, while Doxil clearance is over the timescale of days resulting in a reduction of toxic side-effects. At present it is unclear how doxorubicin is released from Doxil upon accumulation in tumor tissue. However, the present simulations provide a quantitative estimate of the EPR effect, irrespective of the liposomal release mechanism, which is consistent with clinical trial data.

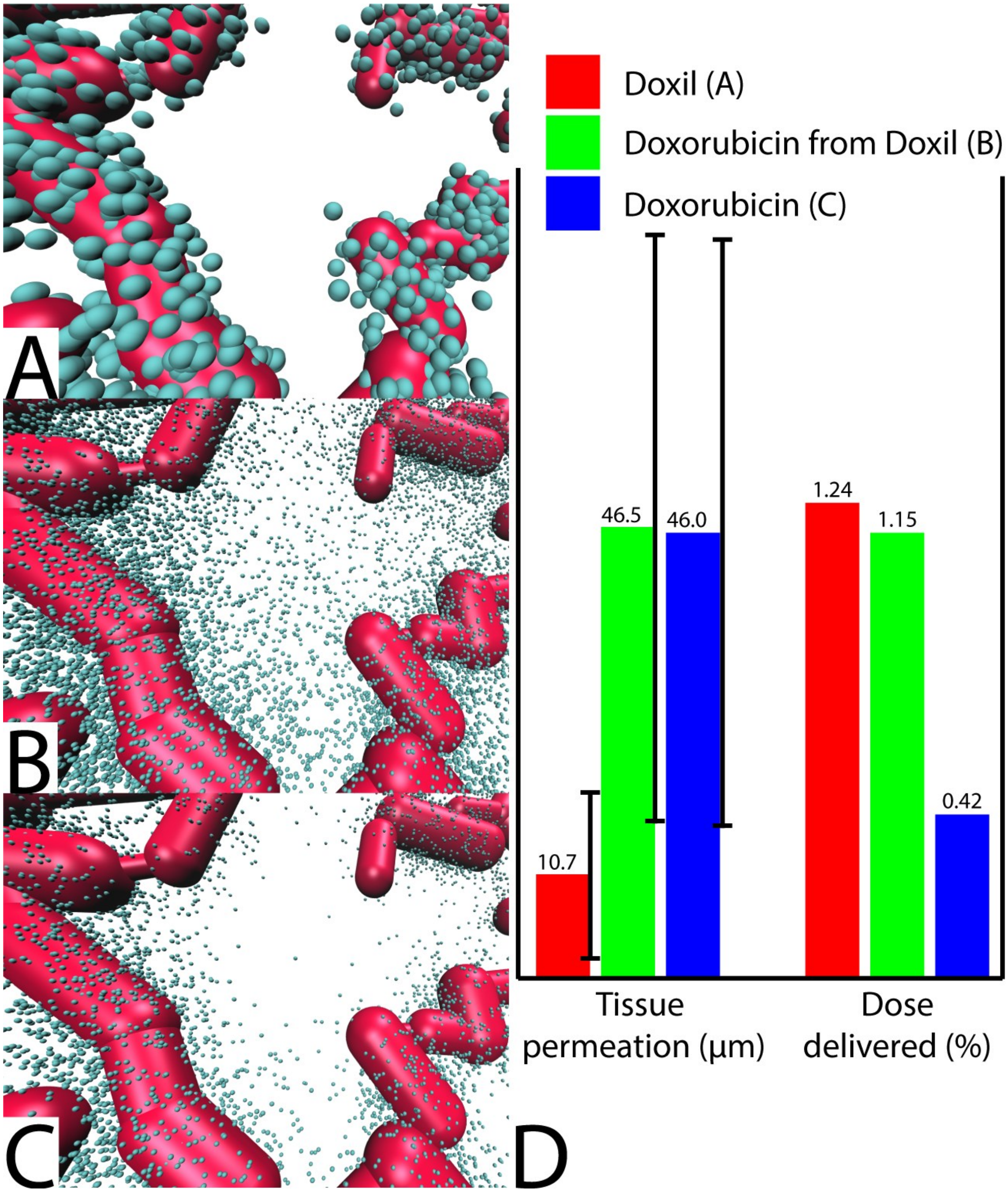

Figure 7 | Comparison of doxorubicin delivery into tumor using direct injection and Doxil after 168 hours. A. This panel shows the final position of doxil liposomes that spontaneously diffused from the vasculature into the tissue after 168 hours. The simulation parameters for Doxil were $D_{vasc} = 1x10^{-6}$ cm^2/s, $D_{tissue} = 1x10^{-12}$ cm^2/s, $k^{eliminiation} = 2.28x10^{-2}$ hr^{-1}, $k_{+}^{tumor} = k_{-}^{tumor} = k^{delivery} = k^{eliminiation}$ x 10^{-2}. **B.** Each of the coordinates from the Doxil simulation in panel A were replaced by 50 doxorubicin clusters, each representing 1000 actual doxorubicin molecules, which were allowed to diffuse until they were cleared from the tumor. The parameters for these doxorubicin molecules are $D_{vasc} = 1x10^{-5}$ cm^2/s, $D_{tissue} = 1x10^{-9}$ cm^2/s, $k^{eliminiation} = 1.57$ hr^{-1}, $k_+^{tumor} = k_-^{tumor} = k^{delivery} = k^{eliminiation}$ x 10^{-2}. **C.** 4,684,500 doxorubicin clusters were injected and equilibrated in the vasculature like in simulation A, and were allowed to diffuse into the tissue. 19,769 doxorubicin clusters reached the tumor compared to 54,065 in simulation B. **D.** Comparison of the mean tissue permeation (i.e. the average distance from each pharmacophore to the nearest vascular segment) and the percentage of initial dose for all three simulations. The percentage of initial dose for B is referenced to the scaled dose of 50 times the dose A in order to capture the number of doxorubicin cleared in blood throughout simulation A, as 97.4% of the doxorubicin clusters which were released from the liposomes of A remained in the tumor tissue. The values for mean tissue permeation of systems A, B, and C, were 11±9 μm, 47±29 μm, and 46±29 μm, respectively. The population standard deviation values are denoted by the vertical black bar centered at each bar. The percentages of doxorubicin molecules reaching the tumor tissue of systems A, B, and C, were 1.24, 1.15, and 0.42, respectively. These results show quantitatively that doxorubicin, due to its small size penetrates much deeper into the tumor tissues than Doxil. However, the much lower clearance rate of Doxil, together with the negligible diffusion back into the vasculature, results in an accumulation of Doxil just beyond the tumor endothelium. This ultimately results in a much higher quantity of doxorubicin delivery into the tumor tissue.

Discussion

The key goal of the present study was to develop a computational model that accurately simulates the delivery of drugs through realistic three-dimensional vascular networks into a solid tumor. Delivery is calculated by tracking the Brownian motion of drug molecules that move freely through the vasculature, across the endothelium, and into tumor tissue. Accurate description of the motion and kinetics by this model requires *a priori* information about the diffusivities of the drugs in blood and tissues, as well as the transport rate across the tumor vessel endothelium. Long timescale simulations also require an estimate of the clearance rate via liver, kidney, macrophages, peripheral tissues, etc.

Diffusion constants for drugs in a tumor have been measured in pre-clinical studies and range from ($D = 10^{-5} – 10^{-9}$ cm^2/s) in rabbits for the small drug doxorubicin HCl (MW = 580 Da)[49] to ($D = 10^{-9} – 10^{-13}$ cm^2/s) for the 100 nm diameter PEGylated liposomal formulation Doxil[37], which encapsulates ~48,000 doxorubicin molecules per liposome[50]. Molecular diffusion constants through the interstitial space of living tissues are more difficult to obtain and are likely to vary between different tissue types. For the present study, I estimated tissue diffusivity for Doxil to be $1\text{x}10^{-12}$ cm^2/s, in line with previous studies[21,33,51]. To investigate the impact of drug weight, size, polarity, and interaction with endothelia and tissue environments, I explored the effect of varying the diffusivity by eight orders of magnitude ($10^{-12} – 10^{-4}$ cm^2/s) (see Figure 4). This suggests that payloads of low therapeutic index should have a tissue diffusivity of at least 10^{-8} cm^2/s to be pharmaceutically effective in penetrating deeply into tumor tissues, depending on the eliminative and distributive half-lives of the drug.

Estimating the transport barrier of drugs across a unit area of tumor vasculature is non-trivial. Transendothelial transport is dominated by the leaky vasculature and hence expected to be similar for most drugs, especially if delivered via a nanoparticle formulation. Varying the transendothelial probability between 10^{-3} – 10^{-5}, a range considerably higher than Doxil's rate-derived parameter of ~6 x 10^{-7} given a simulation time increment of 1 second, indicates that a transport probability exceeding 10^{-4} is desirable for therapeutic efficiency, particularly for slowly diffusing drugs or drug delivery vehicles (see Figure 4).

Simulation of 10^{7} Doxil liposomes diffusing through a realistic tumor vasculature, mapped from a mouse ovarian PET/CT scan image[47], permitted calculation of the percentage of tumor tissues receiving drug doses that fall within the therapeutic window (see Figure 5 of a tumor patch). This revealed that the three-dimensional structure of the vasculature is important for drug delivery efficiency due to two key factors: first, the diameter of the blood vessel scales inversely with the rate of diffusion of drugs into tumor tissues; and secondly, the weighted distance of tissue areas to surrounding capillaries determines the final drug concentration. Both effects depend directly, significantly, and non-trivially on the actual three-dimensional vascular structure.
At present the mechanistic details of how Doxil kills cells via release of its toxic doxorubicin warhead inside the tumor are not fully understood. A typical therapeutic dose of 100 mg Doxil contains roughly 10^{14} liposomes, each containing ~48,000 doxorubicin molecules. Assuming a final tumor delivery range of 0.1% to 1.0% of the administered dose, a 1 cm^{3} tumor, consisting of approximately 10^{9} cells, will take up 10^{11}–10^{12} Doxil liposomes, outnumbering the cells in the tumor by 2–3 orders of

magnitude. Comparison of the delivery of doxorubicin versus Doxil (see Figure 7) suggest a mechanism where Doxil, due to its long half-life, high permeability, and low tissue diffusivity, accumulates just behind the tumor endothelium. Killing of cells buried in the tumor is then achieved by release of doxorubicin, which has a much higher tissue diffusivity than Doxil and is able to penetrate deeply into the tumor without getting cleared by MPS, the kidneys, or the liver. While the simulation does not show how the doxorubicin molecules leave the liposome, it would be consistent with Doxil being taken up by the cell (e.g. via endocytosis), and subsequent release of doxorubicin molecules upon cell death.

The results suggest that other structural features common in tumors, such as necrotic tissues and blood lakes may also be important for predicting how drugs are distributed throughout the tumor tissue. Since the present model assumes no interaction between drug molecules, which is reasonable for liposome-based delivery vehicles as well as typical dosage regimens, the final concentration scales linearly with the initial dosage, allowing extrapolation from computationally feasible to clinically relevant doses. The present model demonstrates that spatial information on the efficiency of drug delivery into target tissues in the body can be obtained using molecular mechanics techniques that track the diffusive motion of individual particles. The key advantage of this approach is that the input parameters are specific to a particular drug or formulation. Once the vascular and tissue diffusivities, transendothelial permeabilities, and pharmacokinetic clearance rates have been determined, the model can be applied to predict the delivery of a drug or drug delivery system to any target tissue for which three-dimensional structural data can be obtained via clinical computed tomography (CT) or other molecular imaging technique. This has a broad range of potential applications including dosage optimization for drugs with small therapeutic windows, which are common in cancer therapy, as well as selecting drugs that have tissue penetration properties that are more suited to a particular tumor. While conventional clinical CT scanners have a typical resolution of 240 µm, too coarse to capture the fine structure of 10-100 µm capillaries inside a tumor, advanced clinical scanners exist which provide resolutions of down to 30 microns[52,53]. For research purposes µCT machines are available with sub-micrometer resolutions, allowing full visualization of even the smallest capillaries. Future improvements in clinical CT and MRI technology will ultimately allow prediction of the optimal drug dosage regimen for a particular patient and target tissue using structural imaging and modeling of drug delivery. At present my methodology can be used to screen the effectiveness and optimize the dose of any medication, especially where uptake into different tissues and microenvironments varies using non-clinical µCT tissue scans.

Chemotherapy outcomes depend critically upon the ability of an anticancer drug to penetrate tumor tissues and cancerous cells at therapeutic concentrations. Systematic optimization of delivery necessitates the development of a more detailed understanding of how drugs enter tissues. The present study shows that there is scope for improvement in the delivery of chemotherapeutics.

References

1. Prokop, A. & Davidson, J. M. Nanovehicular Intracellular Delivery Systems. *J. Pharm. Sci.* **97,** 3518–3590 (2008).

2. Lennard, L. Therapeutic drug monitoring of antimetabolic cytotoxic drugs. *Br. J. Clin. Pharmacol.* **47,** 131–143 (1999).

3. Chatterjee, K., Zhang, J., Honbo, N. & Karliner, J. S. Doxorubicin Cardiomyopathy. *Cardiology* **115,** 155–162 (2010).

4. Perel, P. *et al.* Comparison of treatment effects between animal experiments and clinical trials: systematic review. *BMJ* **334,** 197 (2007).

5. Gao, B., Klumpen, H.-J. & Gurney, H. Dose calculation of anticancer drugs. *Expert Opin. Drug Metab. Toxicol.* **4,** 1307–1319 (2008).

6. Gurney, H. How to calculate the dose of chemotherapy. *Br. J. Cancer* **86,** 1297–1302 (2002).

7. Wallington, M. *et al.* 30-day mortality after systemic anticancer treatment for breast and lung cancer in England: a population-based, observational study. *Lancet Oncol.* **17,** 1203–1216 (2016).

8. Verbraecken, J., Van de Heyning, P., De Backer, W. & Van Gaal, L. Body surface area in normal-weight, overweight, and obese adults. A comparison study. *Metabolism* **55,** 515–524 (2006).

9. Levêque, D. in *Handbook of Anthropometry* (ed. Preedy, V. R.) 1735–1743 (Springer New York, 2012).

10. Chow, D. C., Wenning, L. A., Miller, W. M. & Papoutsakis, E. T. Modeling pO(2) distributions in the bone marrow hematopoietic compartment. I. Krogh's model. *Biophys. J.* **81,** 675–684 (2001).

11. Folkman, J. Role of angiogenesis in tumor growth and metastasis. *Semin. Oncol.* **29,** 15–18 (2002).

12. Folkins, C. & Kerbel, R. S. in *Angiogenesis* (eds. Figg, W. D. & Folkman, J.) 249–258 (Springer US, 2008).

13. Konerding, M. A. *et al.* Evidence for characteristic vascular patterns in solid tumours: quantitative studies using corrosion casts. *Br. J. Cancer* **80,** 724–732 (1999).

14. Folarin, A. A., Konerding, M. A., Timonen, J., Nagl, S. & Pedley, R. B. Three-dimensional analysis of tumour vascular corrosion casts using stereoimaging and micro-computed tomography. *Microvasc. Res.* **80,** 89–98 (2010).

15. Bellone, M. *et al.* The acidity of the tumor microenvironment is a mechanism of immune escape that can be overcome by proton pump inhibitors. *OncoImmunology* **2,** e22058 (2013).

16. Baish, J. W. *et al.* Scaling rules for diffusive drug delivery in tumor and normal tissues. *Proc. Natl. Acad. Sci.* **108,** 1799–1803 (2011).

17. Wojtkowiak, J. W., Verduzco, D., Schramm, K. J. & Gillies, R. J. Drug Resistance and Cellular Adaptation to Tumor Acidic pH Microenvironment. *Mol. Pharm.* **8,** 2032–2038 (2011).

18. Fang, J., Nakamura, H. & Maeda, H. The EPR effect: Unique features of tumor blood vessels for drug delivery, factors involved, and limitations and augmentation of the effect. *Adv. Drug Deliv. Rev.* **63,** 136–151 (2011).

19. Heneweer, C., Holland, J. P., Divilov, V., Carlin, S. & Lewis, J. S. Magnitude of Enhanced Permeability and Retention Effect in Tumors with Different Phenotypes: 89Zr-Albumin as a Model System. *J. Nucl. Med.* **52,** 625–633 (2011).

20. Wong, A. D., Ye, M., Ulmschneider, M. B. & Searson, P. C. Quantitative Analysis of the Enhanced Permeation and Retention (EPR) Effect. *PLOS ONE* **10,** e0123461 (2015).

21. Zhan, W. & Xu, X. Y. A Mathematical Model for Thermosensitive Liposomal Delivery of Doxorubicin to Solid Tumour. *J. Drug Deliv.* **2013,** 1–13 (2013).

22. Rim, J. E., Pinsky, P. M. & van Osdol, W. W. Finite Element Modeling of Coupled Diffusion with Partitioning in Transdermal Drug Delivery. *Ann. Biomed. Eng.* **33,** 1422–1438 (2005).

23. K. Hosie, J. A. Gilbert, D. Kerr, C. Fluid Dynamics in Man of an Intraperitoneal Drug Delivery Solution: 4% Icodextrin. *Drug Deliv.* **8,** 9–12 (2001).

24. Chen, X. B., Lee, H. P., Chong, V. F. H. & Wang, D. Y. A Computational Fluid Dynamics Model for Drug Delivery in a Nasal Cavity with Inferior Turbinate Hypertrophy. *J. Aerosol Med. Pulm. Drug Deliv.* **23,** 329–338 (2010).

25. Jaramillo-Botero, A., Abrol, R., van Duin, A. & Goddard, W. A. in *Nanomedicine - A Systems Engineering Approach* (eds. Zhang, M. & Ning, X.) 245–300 (Pan Stanford Publishing, 2009).

26. Liu, Y., Shah, S. & Tan, J. Computational Modeling of Nanoparticle Targeted Drug Delivery. *Rev. Nanosci. Nanotechnol.* **1,** 66–83 (2012).

27. Doxorubicin Hydrochloride for Injection [patient package insert]. (2013).

28. DOXIL(R) (doxorubicin hydrochloride liposome injection), for intravenous use. [Efficacy-Labeling Change With Clinical Data]. (2015).

29. Gabizon, A. & Papahadjopoulos, D. Liposome formulations with prolonged circulation time in blood and enhanced uptake by tumors. *Proc. Natl. Acad. Sci.* **85,** 6949–6953 (1988).

30. Chouhan, R. & Bajpai, A. Real time in vitro studies of doxorubicin release from PHEMA nanoparticles. *J. Nanobiotechnology* **7,** 5 (2009).

31. Dadsetan, M. *et al.* Controlled release of doxorubicin from pH-responsive microgels. *Acta Biomater.* **9,** 5438–5446 (2013).

32. Modi, S. & Anderson, B. D. Determination of Drug Release Kinetics from Nanoparticles: Overcoming Pitfalls of the Dynamic Dialysis Method. *Mol. Pharm.* **10,** 3076–3089 (2013).

33. Yuan, F. *et al.* Microvascular Permeability and Interstitial Penetration of Sterically Stabilized (Stealth) Liposomes in a Human Tumor Xenograft. *Cancer Res.* **54,** 3352–3356 (1994).

34. Petros, R. A. & DeSimone, J. M. Strategies in the design of nanoparticles for therapeutic applications. *Nat. Rev. Drug Discov.* **9,** 615–627 (2010).

35. Kobayashi, H., Watanabe, R. & Choyke, P. L. Improving Conventional Enhanced Permeability and Retention (EPR) Effects; What Is the Appropriate Target? *Theranostics* **4,** 81–89 (2014).

36. Kumar, R. *et al. In Vivo* Biodistribution and Clearance Studies Using Multimodal Organically Modified Silica Nanoparticles. *ACS Nano* **4,** 699–708 (2010).

37. Toley, B. J., Tropeano Lovatt, Z. G., Harrington, J. L. & Forbes, N. S. Microfluidic technique to measure intratumoral transport and calculate drug efficacy

shows that binding is essential for doxorubicin and release hampers Doxil. *Integr. Biol.* **5,** 1184 (2013).

38. Barapatre, N. *et al.* Quantitative detection of drug dose and spatial distribution in the lung revealed by Cryoslicing Imaging. *J. Pharm. Biomed. Anal.* **102,** 129–136 (2015).

39. Dicheva, B. M. *et al.* Pharmacokinetics, Tissue Distribution and Therapeutic Effect of Cationic Thermosensitive Liposomal Doxorubicin Upon Mild Hyperthermia. *Pharm. Res.* **33,** 627–638 (2016).

40. Sheilagh, B. in *Handbook of Pediatric Transfusion Medicine* 45–61 (Elsevier, 2004).

41. Mintun, M. A. *et al.* Blood flow and oxygen delivery to human brain during functional activity: Theoretical modeling and experimental data. *Proc. Natl. Acad. Sci.* **98,** 6859–6864 (2001).

42. Yoshii, Y. & Sugiyama, K. Intercapillary Distance in the Proliferating Area of Human Glioma. *Cancer Res.* **48,** 2938–2941 (1988).

43. Ciprotti, M. *et al.* Quantitative intratumoural microdistribution and kinetics of 131I-huA33 antibody in patients with colorectal carcinoma. *EJNMMI Res.* **4,** 22 (2014).

44. Carmeliet, P. VEGF as a Key Mediator of Angiogenesis in Cancer. *Oncology* **69,** 4–10 (2005).

45. Bullitt, E. *et al.* Malignancy-Associated Vessel Tortuosity: A Computer-Assisted, MR Angiographic Study of Choroid Plexus Carcinoma in Genetically Engineered Mice. *Am. J. Neuroradiol.* **27,** 612–619 (2006).

46. Shelton, S. E. *et al.* Quantification of Microvascular Tortuosity during Tumor Evolution Using Acoustic Angiography. *Ultrasound Med. Biol.* **41,** 1896–1904 (2015).

47. Nagy, J. A., Chang, S.-H., Dvorak, A. M. & Dvorak, H. F. Why are tumour blood vessels abnormal and why is it important to know? *Br. J. Cancer* **100,** 865–869 (2009).

48. Nagy, J. A. & Dvorak, H. F. Heterogeneity of the tumor vasculature: the need for new tumor blood vessel type-specific targets. *Clin. Exp. Metastasis* **29,** 657–662 (2012).

49. Weinberg, B. D., Patel, R. B., Exner, A. A., Saidel, G. M. & Gao, J. Modeling doxorubicin transport to improve intratumoral drug delivery to RF ablated tumors. *J. Controlled Release* **124,** 11–19 (2007).

50. Abraham, S. A. *et al.* in *Methods in Enzymology* **391,** 71–97 (Elsevier, 2005).

51. Eikenberry, S. A tumor cord model for Doxorubicin delivery and dose optimization in solid tumors. *Theor. Biol. Med. Model.* **6,** 16 (2009).

52. Zagorchev, L. *et al.* Micro computed tomography for vascular exploration. *J. Angiogenesis Res.* **2,** 7 (2010).

53. Starosolski, Z. *et al.* Ultra High-Resolution In vivo Computed Tomography Imaging of Mouse Cerebrovasculature Using a Long Circulating Blood Pool Contrast Agent. *Sci. Rep.* **5,** (2015).

Appendix

Table A1 | Key parameters used in the structural model

Parameter	Value
N_{dose}	$0 – 2 \times 10^{7}$
V_{system}	$1\ mm^{3}$
$D_{vasculature}$ (Doxil)	$1 \times 10^{-6}\ cm^{2}/s$
$D_{vasculature}$ (doxorubicin)	$1 \times 10^{-5}\ cm^{2}/s$
D_{tissue} (Doxil)	$1 \times 10^{-12}\ cm^{2}/s$
D_{tissue} (doxorubicin)	$1 \times 10^{-9}\ cm^{2}/s$
$k^{elimination}$ (Doxil)	0.0204 - 0.0228 (hr^{-1})
$k^{elimination}$ (doxorubicin)	1.56823 (hr^{-1})
k_{+}^{tissue} (Doxil) (Fig 3)	0.0956 (hr^{-1})
k_{-}^{tissue} (Doxil) (Fig 3)	0.198 (hr^{-1})
k_{+}^{tumor} (Doxil)	0.0000228 - 0.00228 (hr^{-1})
k_{-}^{tumor} (Doxil)	0 – 0.00228 (hr^{-1})
k_{+}^{tumor} (doxorubicin)	0.0156823 (hr^{-1})
k_{-}^{tumor} (doxorubicin)	0.0156823 (hr^{-1})
$k^{delivery}$ (Doxil)	0.000228 (hr^{-1})
$k^{delivery}$ (doxorubicin)	0.0156823 (hr^{-1})
$p^{elimination}$ (Doxil)	$5.67 – 6.33 \times 10^{-6}$
$p^{elimination}$ (doxorubicin)	$5.67 – 6.33 \times 10^{-6}$
p_{+}^{tissue} (Doxil) (Fig 3)	2.66×10^{-5}
p_{-}^{tissue} (Doxil) (Fig 3)	5.50×10^{-5}
p_{+}^{tumor} (Doxil)	$6.33 \times 10^{-9} – 6.33 \times 10^{-7}$
p_{-}^{tumor} (Doxil)	$0 – 6.33 \times 10^{-7}$
p_{+}^{tumor} (doxorubicin)	64.36×10^{-6}
p_{-}^{tumor} (doxorubicin)	4.36×10^{-6}
$p^{delivery}$ (Doxil)	6.33×10^{-8}
$p^{delivery}$ (doxorubicin)	4.36×10^{-6}

N_{dose} = Number of liposomes simulated during the majority of the study, V_{system} = simulated volume of tissue and vasculature. $D_{vasculature}$ = diffusion coefficient of therapeutics in the vasculature, D_{tissue} = diffusion coefficient of therapeutics in the both tumorous and healthy tissues, $k^{elimination}$ = first-order rate constant for eliminating therapeutics from the system, k_{+}^{tissue} = first-order rate constant for therapeutics to transfer from blood to peripheral tissues, k_{-}^{tissue} = first-order rate constant for therapeutics to transfer from peripheral tissues to blood, k_{+}^{tumor} = first-order rate constant for therapeutics to transfer from blood to tumor, k_-^{tumor} = first-order rate constant for therapeutics to transfer from tumor to blood, $k^{delivery}$ = first-order rate constant for therapeutics to finish releasing their payload within the tumor, $p^{elimination}$ = per-particle Monte Carlo elimination probability within a simulation time-step of one second. p_+^{tissue} = per-particle Monte Carlo probability of transfer between blood and peripheral tissue within a simulation time-step of one second. p_-^{tissue} = per-particle Monte Carlo probability of transfer between peripheral tissue and blood within a simulation time-step of one second. p_+^{tumor} = per-particle Monte Carlo probability of transfer between blood and tumor tissue within a simulation time-step of one second. p_-^{tumor} = per-particle Monte Carlo probability of transfer between tumor tissue and blood within a simulation time-step of one second $p^{delivery}$ = Monte Carlo probability of completed delivery to tumor within a simulation time-step of one second.

Table A2 | Parameters for system 1 (parallel capillaries Figure 2A)

Parameter	**Value**
Number of cylinders	36
Inter-capillary spacing of vessel array 1 (sufficient)	50.0 µm
Inter-capillary spacing of vessel array 2 (insufficient)	100.0 µm
Maximum vessel width	37.0 µm
Minimum vessel width	10.0 µm
Average vessel width	17.9 µm
Standard deviation of vessel width	7.0 µm
Maximum vessel length	115.0 µm
Minimum vessel length	370.7 µm
Average vessel length	211.8 µm
Standard deviation of vessel length	80.4 µm
Maximum vessel surface area	5.42×10^3 µm^2
Minimum vessel surface area	3.49×10^4 µm^2
Average vessel surface area	1.12×10^4 µm^2
Standard deviation of vessel surface area	5.64×10^3 µm^2
Maximum vessel volume	2.03×10^4 µm^3
Minimum vessel volume	2.62×10^5 µm^3
Average vessel volume	5.58×10^4 µm^3
Standard deviation of vessel volume	5.08×10^4 µm^3

System 1 was inspired to test the simple effect on intercapillary distance on the simultaneous therapeutic uptake of the surrounding tissues. The widths were based on textbook values which agree to data obtained within existing micrographs of human microvasculature[13,14,46]. The other parameters are calculated using only the information obtained from the cylindrical segments of the vessels (i.e. the spherical joints are ignored).

Table A3 | Parameters for system 2 (simple microtumor Figure 2B)

Parameter	**Value**
Number of cylinders	24
Minimum vessel width	10.0 μm
Maximum vessel width	37.0 μm
Average vessel width	14.0 μm
Standard deviation of vessel width	7.7 μm
Minimum vessel length	50.0 μm
Maximum vessel length	316.2 μm
Average vessel length	133.7 μm
Standard deviation of vessel length	59.8 μm
Minimum vessel surface area	1.57×10^3 μm^2
Maximum vessel surface area	2.78×10^4 μm^2
Average vessel surface area	6.48×10^3 μm^2
Standard deviation of vessel surface area	6.15×10^3 μm^2
Minimum vessel volume	3.93×10^3 μm^3
Maximum vessel volume	1.95×10^5 μm^3
Average vessel volume	3.29×10^4 μm^3
Standard deviation of vessel volume	5.31×10^4 μm^3

System 2 was inspired to be a simple microtumor with only a few branches from a source arteriole and leading into a draining venule. The widths were based on textbook values which agree to data obtained within existing micrographs of human microvasculature[13,14,46]. The other parameters are calculated using only the information obtained from the cylindrical segments of the vessels (i.e. the spherical joints are ignored).

Table A4 | Parameters for system 3 (planar capillary Figure 2C)

Parameter	**Value**
Number of cylinders	48
Minimum vessel width	10.0 μm
Maximum vessel width	10.0 μm
Average vessel width	10.0 μm
Standard deviation of vessel width	0.0 μm
Minimum vessel length	55.9 μm
Maximum vessel length	293.4 μm
Average vessel length	145.3 μm
Standard deviation of vessel length	54.5 μm
Minimum vessel surface area	1.76×10^3 μm^2
Maximum vessel surface area	9.22×10^3 μm^2
Average vessel surface area	4.57×10^3 μm^2
Standard deviation of vessel surface area	1.71×10^3 μm^2
Minimum vessel volume	4.39×10^3 μm^3
Maximum vessel volume	2.30×10^4 μm^3
Average vessel volume	1.14×10^3 μm^3
Standard deviation of vessel volume	4.28×10^3 μm^3

System 3 is motivated to be a simple planar capillary mesh, in which flow directions would be difficult to calculate using continuum methods. The widths were chosen to be uniform with a value that exists within existing micrographs of human endothelia[13,14,46]. The other parameters are calculated using only the information obtained from the cylindrical segments of the vessels (i.e. the spherical joints are ignored).

Table A5 | Parameters for system 4 (mouse ovarian tumor Figure 5).

Parameter	**Value**
Number of cylinders	201
Minimum vessel width	5.1 μm
Maximum vessel width	19.9 μm
Average vessel width	12.8 μm
Standard deviation of vessel width	4.48 μm
Minimum vessel length	10.5 μm
Maximum vessel length	180.4 μm
Average vessel length	43.7 μm
Standard deviation of vessel length	26.9 μm
Minimum vessel surface area	2.27×10^{2} μm^{2}
Maximum vessel surface area	5.81×10^{3} μm^{2}
Average vessel surface area	1.74×10^{3} μm^{2}
Standard deviation of vessel surface area	1.18×10^{3} μm^{2}
Minimum vessel volume	3.14×10^{2} μm^{3}
Maximum vessel volume	2.68×10^{4} μm^{3}
Average vessel volume	6.22×10^{3} μm^{3}
Standard deviation of vessel volume	5.40×10^{3} μm^{3}

System 4 was generated by hand-tracing coordinates in a plane over the image provided from a PET image of an ovarian mouse tumor[47]. The widths were scaled programmatically and by eye to match the outline of the blood vessels, but better algorithms need to be developed in further studies of realistic vasculature. The other parameters are calculated using only the information obtained from the cylindrical segments of the vessels (i.e. the spherical joints are ignored).

Curriculum vitae

Evan P. Troendle

Born 14th January, 1992 in Cedar Rapids, IA

Education

King's College London – London, UK (July 2017 – current)

PhD chemistry

Johns Hopkins University – Baltimore, Maryland (September 2014 – May 2017)

MSE materials science and engineering

Coe College – Cedar Rapids, Iowa (August 2010 – May 2014)

BA double major: physics, music; double minor: mathematics, computer science

Research Experience

King's College London Department of Chemistry (July 2017 - current) molecular mechanics (computational) with Dr. Martin Ulmschneider

Johns Hopkins University Department of Materials Science and Engineering (September 2014 - May 2017) molecular mechanics (computational) with Dr. Martin Ulmschneider

Coe College Physics Department (May 2011 – May 2014) glass science (computational and experimental) with Dr. Steve Feller

Universidade Federal de São Carlos (UFSCar) Departamento de Engenharia de Materiais (Summer 2013) glass rheology (experimental) with Dr. Edgar Zanotto

University of Warwick Department of Physics (Summer 2012) glass nuclear magnetic resonance (NMR) (experimental) with Dr. Diane Holland

Grants & Scholarships

Johns Hopkins University Dean's Fellowship (2014-2017)

International Materials Institute for New Functionality in Glass (IMI-NFG) International Research Grant (2013)

R. J. McElroy Student/Faculty Research Grant (2012)

Selected Publications

Predicting drug delivery efficiency into tumor tissues through molecular simulation of diffusion in complex vascular networks

Pending publication

The transport mechanisms, free energy barrier profiles, and kinetics of small-molecule diffusion across membranes of the blood brain barrier

Pending publication

An anomaly in the glass transition width trends of alkali borate glasses at low modifier loadings

Pending publication

A 10B NMR study of trigonal and tetrahedral borons in ring structured borate glasses and crystals

Physics and Chemistry of Glasses - European Journal of Glass Science and Technology Part B, Volume 56, Number 5, October 2015, pp. 177-182(6)

Characterization of 1800 Hamamatsu R7600-M4 PMTs for CMS HF Calorimeter upgrade

Journal of Instrumentation, Volume 9, Issue T06005, 06/2014. IOP Publishing Ltd

Structure and Properties of Barium and Calcium Borosilicate Glasses

Physics and Chemistry of Glasses - European Journal of Glass Science and Technology Part B, Volume 53, Number 5, October 2012, pp. 210-218(9)

SpectraFit: a new program to simulate and fit distributed 10B powder patterns–application to symmetric trigonal borons

Physics and Chemistry of Glasses - European Journal of Glass Science and Technology Part B, Volume 53, Number 3, June 2012, pp. 121-127(7)

Teaching Experience

TA - EN.510.312 Thermodynamics of Materials (Fall 2016, Spring 2017) with Dr. Martin Ulmschneider

TA - EN.510.426 Biomolecular Materials – Soluble Proteins and Amphiphiles (Fall 2016) with Dr. Kalina Hristova

TA - EN.510.602 Thermodynamics of Materials (Fall 2015) with Dr. Michael Falk

TA - EN.510.202 Computation and Programming for Materials Scientists and Engineers (Spring 2015) with Dr. Martin Ulmschneider